

Simulation of single-mode high-power semiconductor lasers

Hans Wenzel and Götz Erbert

Ferdinand-Braun-Institut für Höchstfrequenztechnik
Rudower Chaussee 5, D-12489 Berlin, Germany.

ABSTRACT

Theoretical studies of aluminum-free RISAS and ARROW type lasers operating at 800 nm and 940 nm, respectively, are presented. At 800 nm, the electron leakage current over the hetero barriers leads to a sub-linear light-current characteristic. In order to obtain a high output power at moderate currents, either the losses must be kept as small as possible, or the barriers for the electrons must be increased, for example by higher p-doping. At 940 nm, the leakage current is not as problematic. In both RISAS and ARROW lasers, excess loss for the higher-order modes is needed to prevent them from lasing. The theoretical maximum single mode power of ARROW lasers obtained with a two-dimensional FEM-solution of the scalar wave equation is lower than found with the effective index method.

Keywords: simulation, semiconductor transport equations, high-power lasers, spatial holeburning, carrier leakage

1. INTRODUCTION

High-output-power semiconductor lasers emitting in a single transverse mode are promising for end-pumping of solid-state lasers and rare-earth-doped fiber amplifiers. In this relation the aluminum-free material system InGaAsP grown on GaAs substrates is especially interesting because it has a number of superior properties compared to the AlGaAs system such as no surface oxidation and less crystal defects (donor-related deep traps, dark-line defects).¹⁻³ This promises a more stable two-step epitaxy for growing buried laser structures and a higher resistance to the catastrophic optical damage (COD).

In this paper we present theoretical results for two different Al-free buried structures, namely a real-index guided self-aligned structure (RISAS)⁴ operating at 800 nm and an anti-resonant reflecting optical waveguide (ARROW)⁵ structure operating at 940 nm. With a RISAS laser made from AlGaAs/GaAs, Imafuji *et al.*⁴ obtained a maximum single-mode output power of 600 mW. It has been proposed that the ARROW lasers yield even higher single-mode output power due to a special waveguiding mechanism.

For a semiconductor laser, the coupled system of equations for the charged carriers and the optical field has to be solved in three spatial dimensions. For simulating the carrier transport, sophisticated simulators⁷⁻¹⁰ use the continuity equations for the electron, hole and energy current densities and the Poisson equation for the electrostatic potential. The optical field distribution is determined by solving a scalar wave equation. In general, these equations are only solved in the (transverse) plane perpendicular to the wave propagation. But because lasers are three-dimensional in nature, a simple rate equation for the optical power is usually added which is solved self-consistently with the other equations. Longitudinal varying structures, for example, due to longitudinal spatial holeburning or due to tapered stripe contacts can not be dealt with in this approach.

In quantum well (QW) lasers, additionally the Schrödinger equation and quantum kinetic equations describing the

capture of electrons and holes into the QWs have to be solved. In this paper, we treat the active QWs as classical regions characterized by effective parameters. A more correct treatment of active QWs is under way. However, we believe that this improvement will not change the basic trends predicted in this paper.

The paper is organized as follows. The theoretical laser model is introduced in Section 2. The material functions and parameters occurring in the model are given in Section 3. Our device examples and the modeling results are presented in Section 4. Finally, results are summarized in Section 5.

2. MODEL

Our theoretical model underlying the calculations follows the scheme presented for the first time by Wünsche *et al.*⁶ We consider laser structures having almost no *built-in* longitudinal variation and which lengths are much larger than the transverse dimensions. Therefore, the carrier transport equations and the optical wave equation need to be solved only in the transverse plane of the device. The set of transverse equations depends parametrically on the longitudinal coordinate z , but not explicitly. Instead, this dependence is mediated by the optical power. Because we confine ourselves to the stationary case, in the transverse calculation the optical power P can be treated as an external parameter similarly as the applied voltage U . In this step, there is no need for an additional equation for P self-consistently to be solved with the other equations.

We use the program ToSCA^{11,12} which is based on the finite element method (FEM) for solving the following set of partial differential equations in the transverse plane of the laser: the Poisson equation,

$$\epsilon_0 \nabla_t \epsilon_s \nabla_t \phi = e(n - p + C) \quad (1)$$

(ϵ_s static dielectric constant, ϕ electrostatic potential, n, p electron and hole density, respectively, C charged impurity density), the continuity equations for the electron and hole current densities

$$\nabla_t \mu_n n \nabla_t F_n = e(R + R_{stim}) \quad (2)$$

$$-\nabla_t \mu_p p \nabla_t F_p = e(R + R_{stim}) \quad (3)$$

(μ mobility, F quasi-Fermi energy, R radiative spontaneous and non-radiative recombination rate, R_{stim} stimulated recombination rate), and the waveguide equation

$$\left[\nabla_t^2 + \frac{\omega_v^2}{c^2} \epsilon(\mathbf{r}, \omega_v) \right] \Phi_v(\mathbf{r}) = \beta_v^2 \Phi_v(\mathbf{r}) \quad (4)$$

(v transverse mode index, ω_v optical circular frequency of lasing ($v = 0$) and non-lasing modes, Φ_v transverse electric field distribution (suitably normalized), β_v complex propagation constant). Carrier transport and optical waveguiding are coupled via the stimulated recombination rate

$$R_{stim} = \frac{c\epsilon_0}{2\hbar\omega_P} n_r(\mathbf{r}, \omega_P) g(\mathbf{r}, \omega_P) |\Phi_0(\mathbf{r})|^2 P \quad (5)$$

(n_r refractive index, g optical gain) and the complex dielectric function ϵ of the pumped laser cavity. In Eq. (5) we dropped the sum over different modes. This means, that we consider only one lasing mode (the mode $v=0$) and neglect the power carried by all other modes. The quasi-Fermi energies F_n and F_p are linked with the carrier densities n and p , respectively, by means of the Fermi-Dirac statistics.

Equations (1)-(4) have to be supplemented by boundary conditions as well as matching conditions at the heterointerfaces for which the reader is referred to Gajewski *et al.*¹¹ We remark that in ToSCA continuity of the quasi-Fermi energies at the heterointerfaces is assumed. This allows us to handle abrupt and graded interfaces on equal footing. The waveguide equation is solved by inverse vector iteration using homogeneous Dirichlet or Neumann conditions (at symmetry planes). This method is very fast for calculating a desired eigenvalue which is in our case the complex propagation constant β . However,

in ToSCA only the real part of the dielectric function is accounted for in the iteration, the imaginary part of ϵ is treated perturbationally.

Because in this paper we focus on the electro-optical behavior of laser structures, we have omitted the continuity equation for the energy density working with a constant temperature in the devices. This means, that the results are only valid for pulsed or quasi-cw operation of the lasers. The longitudinal spatial homogeneity is broken by the laser facets. The correct treatment of the region near the laser facet where enhanced surface recombination occurs is not the scope of this paper. The power loss at the facets is taken into account in the next step (*cf.* Eq. (7)). As well known, the associated inhomogeneous power distribution leads to an inhomogeneous distribution of the carrier densities in the longitudinal direction due to stimulated recombination (socalled longitudinal spatial holeburning, LSB). LSB is modelled via the dependence of β on P as shown below. The small gradients of the carrier densities introduced by LSB can be neglected.

Equations (1)-(4) are solved for different values of U , P , ω_0 and ω_v . The results (e.g., the contact current per laser length and β_v) are stored in a look-up table which is then used to calculate the optical power-current (P-I) characteristics. For a Fabry-Perot (FP) laser the longitudinal power distributions of the forward (P^+) and backward (P^-) travelling waves are obtained from the ordinary differential equations:

$$\frac{dP_v^\pm}{dz} = \pm [2\text{Im}(\beta_v(U, P, \omega_0, \omega_v)) - \alpha_0] P_v^\pm \quad (6)$$

with $P = P_0^+ + P_0^-$ and where $\omega_0 = \omega_v$ for the lasing mode and $\omega_v \neq \omega_0$ for all other modes. The loss coefficient α_0 includes all loss mechanisms which are not already accounted for in the imaginary part of β , such as absorption or scattering loss. The equations (6) have to be solved subject to the boundary conditions:

$$P_v^+(0) = R_0 P_v^-(0) \quad \text{and} \quad P_v^-(L) = R_L P_v^+(L), \quad (7)$$

(R_0, R_L facet reflectivities). Because the phase of the optical field does not enter (6), we have to formulate one additional equation. In spatially homogeneous FP lasers the maximum of the optical gain $g(\omega)$ determines the lasing frequency. It can be shown, that in spatially non-homogeneous FP lasers this means that the maximum of the integral

$$\int_0^L \text{Im}(\beta_v) dz \quad (8)$$

with respect to ω_0 or ω_v has to be found. Note, that the frequencies of the non-lasing modes are in fact complex. The imaginary part of ω_v gives the damping constant of the corresponding mode.⁶ In spatial homogeneous lasers, the damping constant is proportional to the gain difference between the modes. The lasing mode is the first mode for which the damping constant becomes zero if the gain in the laser resonator is increased.

To summarize, solving Eqs. (6) and (8) self-consistently yields for a given applied voltage the output power and the wavelength of the lasing mode and the damping constants and wavelengths of the non-lasing modes. A jump to another mode or multimode operation possibly connected with a kink in the P-I characteristics occurs, if the damping constant of at least one of the non-lasing modes vanishes. Our theoretical model is now complete and we can specify the material functions and parameters entering the model.

3. MATERIAL FUNCTIONS

The electron and hole mobilities are assumed to be constant with the values $\mu_n = 4000 \text{ cm}^2/\text{Vs}$ and $\mu_p = 100 \text{ cm}^2/\text{Vs}$ in the conductive regions. The recombination rate is given by the expression

$$R = \frac{np - n_0 p_0}{\tau_n(p + p_i) + \tau_p(n + n_i)} + (B + C_n n + C_p p)(np - p_0 n_0) \quad (9)$$

with $\tau_n = \tau_p = 3 \text{ ns}$ (recombination via deep centers (Shockley-Read-Hall recombination)), $B = 10^{-10} \text{ cm}^3/\text{s}$ (radiative spontaneous recombination) and $C_n = C_p = 2 \cdot 10^{-30} \text{ cm}^6/\text{s}$ (Auger recombination). In Eq. (9) the equilibrium densities n_0

and p_0 which are identical to the intrinsic densities n_i and p_i in the case of Boltzmann statistics ensure that the recombination rate vanishes in thermal equilibrium.

The complex dielectric function is modeled as

$$\varepsilon(n, p, \omega) = \left[n_r - n'_r \left(\frac{n+p}{2} - C \right) + \frac{ic}{2\omega} g(n, p, \omega) \right]^2 \quad (10)$$

with n_r given in Table 1 and $n'_r = 10^{-20} \text{cm}^3$ if not stated otherwise. The optical gain g is zero outside the active QWs and depends both on the carrier densities and the optical frequency. As mentioned above, it is approximately the maximum of g which determines the lasing frequency (or wavelength). In this paper, we omit the dispersion of g working with fixed lasing wavelengths of $\lambda_0 = 800 \text{ nm}$ (RISAS) and $\lambda_0 = 940 \text{ nm}$ (ARROW). The dependence of the optical gain on the carrier densities is given by the expression

$$g(n, p) = g_0 \cdot \left[\exp \left(\frac{F_n(n) - F_p(p)}{kT} \right) - 1 \right] \cdot \frac{1}{1 + \exp \left(\frac{F_n(n) - E_c}{kT} \right)} \cdot \frac{1}{1 + \exp \left(\frac{E_v - F_p(p)}{kT} \right)} \quad (11)$$

(E_c, E_v conduction and valence band edges including the contribution of the electro-static potential).

The factor g_0 as well as the effective band edge density of states (DOS) in the respective active QW are obtained as follows. First the conduction band DOS is calculated as described in Ref.¹³ assuming parabolic conduction subbands. Second, the valence band DOS is determined in such a way that the transparency carrier density is the same as obtained from a $\mathbf{k} \cdot \mathbf{p}$ valence bandstructure calculation using a $4 \cdot 4$ Hamiltonian.¹⁴ Third, g_0 is used to fit the gain function (11) to the optical gain curve obtained with the $\mathbf{k} \cdot \mathbf{p}$ model. Together with the effective band edge density of states listed in Table 1, we obtained $g_0 = 3000 \text{ cm}^{-1}$ for a 15 nm thick $\text{Ga}_{0.63}\text{In}_{0.37}\text{As}_{0.48}\text{P}_{0.52}$ QW ($\lambda_p \approx 800 \text{ nm}$) as used for the RISAS laser and $g_0 = 7400 \text{ cm}^{-1}$ for a 5 nm thick $\text{In}_{0.15}\text{Ga}_{0.85}\text{As}$ QW ($\lambda_p \approx 940 \text{ nm}$) embedded in GaAs as used for the ARROW laser, cf. Fig. 1. Note, that in the transverse calculation we dropped the intra-band absorption proportional to the carrier densities. Instead, we put all losses including absorption loss into α_0 . This allows us to vary α_0 without having to repeat the time-consuming transverse calculation.

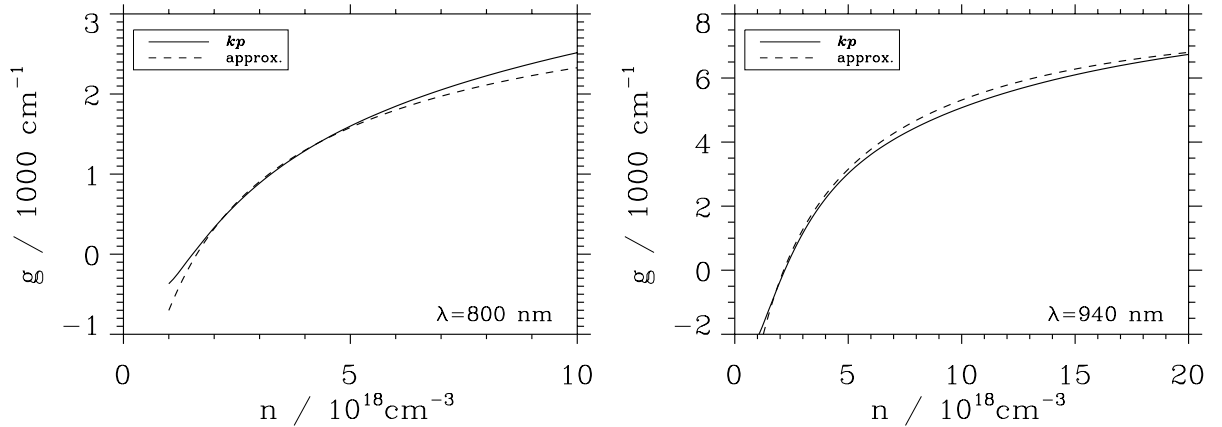


Figure 1: Gain versus carrier density ($n = p$ assumed) for the RISAS (left) and the ARROW laser (right) as used in the simulations. Solid: Obtained by microscopic model¹⁴ (fixed wavelength near gain maximum). Dashed: Expression (11).

A crucial point in the simulation of the current flow are the band discontinuities. Due to the quite different masses of electrons and holes, not only the band gap differences are important, but also how they are distributed between the conduction and valence bands. We use a modified model after van de Walle¹⁵ for calculating the band offsets modified taking into account quantization effects in QWs. The material parameters used in the calculations are summarized in Table 1.

	E_g/eV	E_c/eV	N_c/cm^{-3}	N_v/cm^{-3}	$n_r(800 \text{ nm})$	$n_r(940 \text{ nm})$	ϵ_s
InGaP	1.901	0.000	$1.13 \cdot 10^{18}$	$2.26 \cdot 10^{19}$	3.295	3.234	11.725
InGaAsP	1.853	-0.013	$1.08 \cdot 10^{18}$	$2.16 \cdot 10^{19}$	3.333	3.269	11.871
GaAs	1.425	-0.089	$4.34 \cdot 10^{17}$	$1.45 \cdot 10^{19}$	3.670	3.548	13.100
active (RISAS)	1.55	-0.122	$9.60 \cdot 10^{17}$	$5.50 \cdot 10^{18}$	3.609	—	12.577
active (ARROW)	1.32	-0.139	$1.35 \cdot 10^{18}$	$7.00 \cdot 10^{18}$	—	3.665	13.325

Table 1: Energy gaps, conduction band edges, conduction- and valence band edge densities of states, refractive indices and static dielectric constants used in the calculations.

4. RESULTS

In this Section, we show calculated P-I characteristics in dependence of various parameters. Our standard device is 1 mm long with power reflectivities of 10% and 90% at the end facets and has internal losses of $\alpha_0 = 5 \text{ cm}^{-1}$ if not specified otherwise. The output power is taken at the facet with the lower reflectivity.

4.1. RISAS laser

As found both experimentally and theoretically,¹⁶ the electron leakage current over the hetero barriers is a serious problem in aluminum-free InGaAsP lasers emitting around 800 nm. The reason is, that in this material system in contrast to the AlGaAs system the conduction band discontinuity is usually much smaller than the valence band discontinuity, *cf.* Table 1.

Here we want to investigate what the implications of this fact are for single-mode high-power lasers. In order to diminish the leakage current, one could first exchange the bulk active layer used in Ref.¹⁶ by compressively strained single or multi QWs. Tensile strain is not promising due to the staggered alignment in this case (type II QWs).¹⁷ In this paper, we take as active region a 15 nm thick single compressively strained InGaAsP QW (*cf.* Sect. 3.) sandwiched by InGaAsP waveguide and InGaP cladding layers. A comparison of different active layer compositions to achieve a lasing wavelength of 800 nm is subject of further studies.

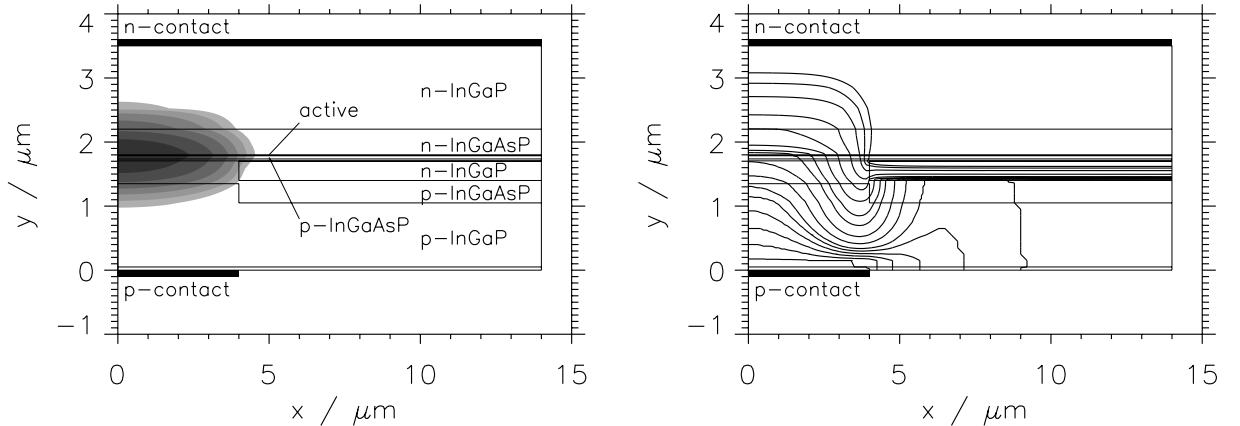


Figure 2: Cross-section of the optimized RISAS laser and distributions of the intensity of the fundamental lasing mode (left) and the hole quasi-Fermi energy (right) near threshold. In the left gray-scale plot, the darkest region corresponds to the highest mode intensity which changes by a factor 1/2 from contour line to contour line. In the right part, contour lines are drawn between -1.58 eV at the p-contact and -1.54 eV in non-equidistant steps.

The cross-section of the RISAS laser underlying the transverse simulation is depicted in Fig. 2. At $x = 0$, there is a symmetry plane. The total core width of our example device is $8 \mu\text{m}$ if not specified otherwise and the effective index step is approximately $4 \cdot 10^{-3}$. The aim of the lateral n-doped InGaP layer is two-fold: Due to its lower refractive index than the surrounding material, it leads to real index guiding in the lateral direction, and due to the reverse biased pn-junction, current confinement is provided. As an example, in Fig. 2 contour plots of the distributions of the intensity of the lasing mode and the electro-chemical potential of the holes near threshold are shown. Note, that the current flows perpendicular to the contour lines of the potential. The impact of the reverse-biased pn-junction is clearly seen.

In Fig. 3 the influence of decreasing the core width on the P-I characteristic is depicted. The bending of the curves is due to the electron leakage current which is the larger the smaller the core width is. The reason for this behavior is the enhanced lateral spatial holeburning.

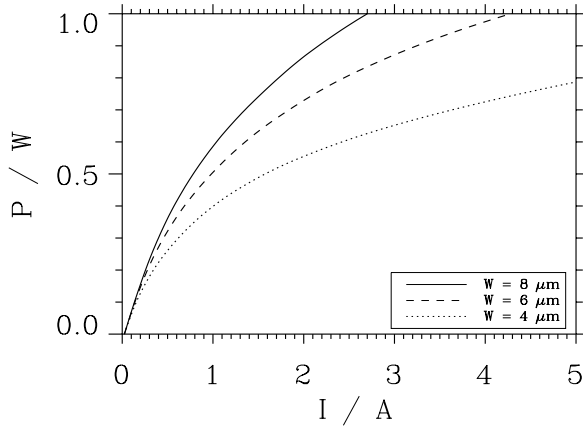


Figure 3: Output power of the RISAS laser versus current for different values of the core width. Solid: $W = 8 \mu\text{m}$, dashed: $W = 6 \mu\text{m}$, dotted: $W = 4 \mu\text{m}$. In this figure, the differential index n'_l was set to zero.

In Figs. 4 and 5 the influence of internal losses and the laser lengths on the P-I characteristics is shown. The larger the internal losses, the higher the voltage to be applied between the contacts, and the smaller the barriers for the minority electrons at higher output power (*cf.* Fig. 9). This leads to a decrease of the internal quantum efficiency because more and more electrons do not recombine radiatively in the active QW but recombine non-radiatively in the p-doped waveguide and cladding layers. The same holds for the dependence on the laser length for higher output power, because the outcoupling loss is smaller for longer lasers. However, at lower output power the situation is different, because in general the threshold current increases and the external efficiency decreases with increasing laser length (*cf.* the inset in Fig. 5). Note, that for our particular choice of the parameters (reflectivities and internal losses), it does not make sense to make the laser longer than 1 mm. The reason is, that α_0 becomes the dominant loss mechanism.

In the P-I characteristics shown until now, only the fundamental mode is taken into account. However, this does not mean that the fundamental mode is the only one that lases. In Fig. 6 the kink power is depicted, where due to (lateral) spatial holeburning the first order mode displayed in a gray-scale plot in Fig. 7 is no longer damped and starts to lase. For equal losses of the fundamental and first order mode ($\Delta\alpha = 0$), the kink power is less than 100 mW. However, in reality the losses of the higher order modes are usually larger because they experience, *e.g.*, more scattering loss due to interface roughness at the etched interfaces (*cf.* Fig. 7). As one can see from Fig. 6, an additional loss of $\Delta\alpha = 10 \text{ cm}^{-1}$ is needed for internal losses of $\alpha_0 = 5 \text{ cm}^{-1}$ common for both modes to get single-mode operation for more than 500 mW. The kink power decreases for increasing internal loss due to increased spatial holeburning.

Until now, we reported results for a structure having relatively low acceptor densities of $N_A = 2 \cdot 10^{17} \text{ cm}^{-3}$ and $N_A = 5 \cdot 10^{17} \text{ cm}^{-3}$ in the waveguide layer and in the adjacent part of the cladding layer, respectively. This is done to keep the active region free of point defects, and to lower the free carrier absorption. For AlGaAs lasers emitting at 980 nm, this was shown to yield very high external efficiencies.¹⁸ But in the InGaAsP system and for smaller wavelengths possibly higher p-doping is essential to increase the internal efficiency. This is shown in Fig. 8. Especially an enhanced p-doping of the waveguide layer acts most effectively (dotted line in Fig. 8).

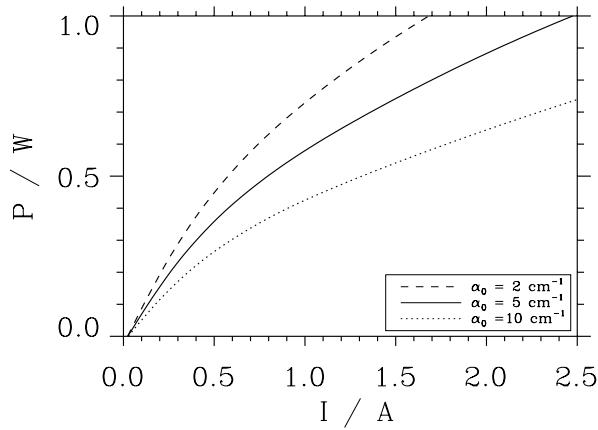


Figure 4: Output power of the RISAS laser versus current for different values of the internal losses. Solid: $\alpha_0 = 5 \text{ cm}^{-1}$, dashed: $\alpha_0 = 2 \text{ cm}^{-1}$, dotted: $\alpha_0 = 10 \text{ cm}^{-1}$

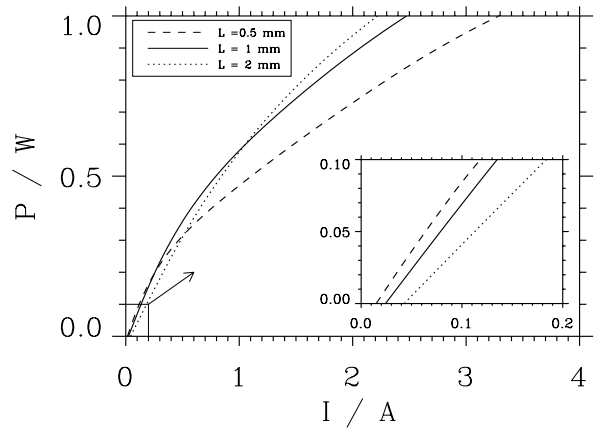


Figure 5: Output power of the RISAS laser versus current for different values of the laser length. Solid: $L = 1 \text{ mm}$, dashed: $L = 0.5 \text{ mm}$, dotted: $L = 2 \text{ mm}$.

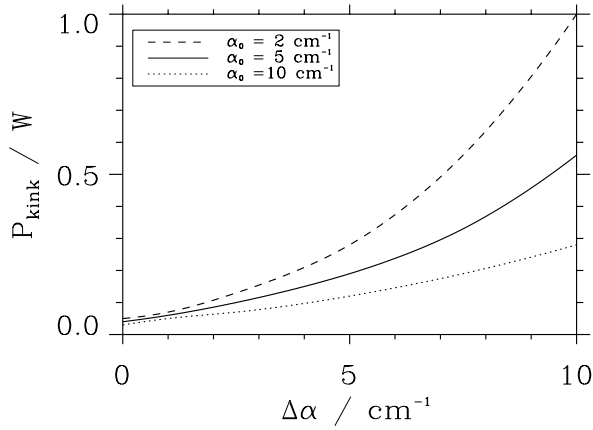


Figure 6: Kink power of the RISAS laser versus loss difference for the same values of the internal losses as in Fig. 4.

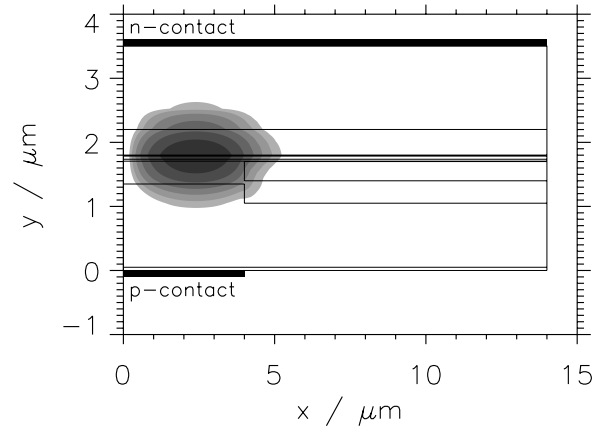


Figure 7: Gray-scale plot of the intensity distribution of the first order RISAS mode possibly competing with the lasing mode at higher output power.

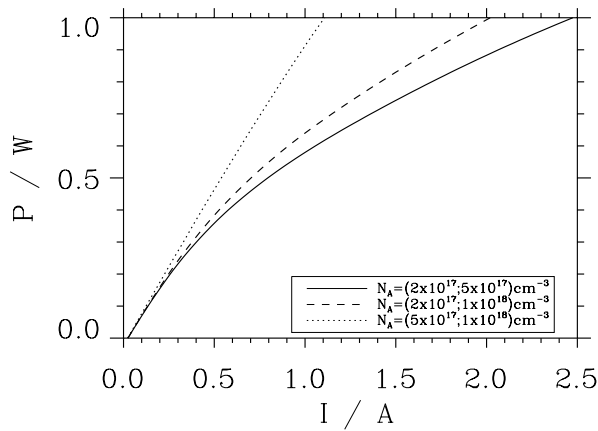


Figure 8: Output power of the RISAS laser versus current for different p-doping profiles just above the active QW. Solid: $N_A = 2 \cdot 10^{17} \text{ cm}^{-3}$ (waveguide), $N_A = 5 \cdot 10^{17} \text{ cm}^{-3}$ (cladding). Dashed: $N_A = 2 \cdot 10^{17} \text{ cm}^{-3}$ (cladding), $N_A = 1 \cdot 10^{18} \text{ cm}^{-3}$ (waveguide). Dotted: $N_A = 5 \cdot 10^{17} \text{ cm}^{-3}$ (waveguide), $N_A = 1 \cdot 10^{18} \text{ cm}^{-3}$ (cladding).

The impact of various p-doping profiles on the barriers for the minority electrons is depicted in Fig. 9 near threshold and at a optical power of 1 W somewhere in the resonator. For a weak p-doping (solid line), the barrier at 1 W is strongly reduced compared to threshold leading to a strongly increased electron leakage. An enhancement of the p-doping almost preserves the barrier (dotted line).

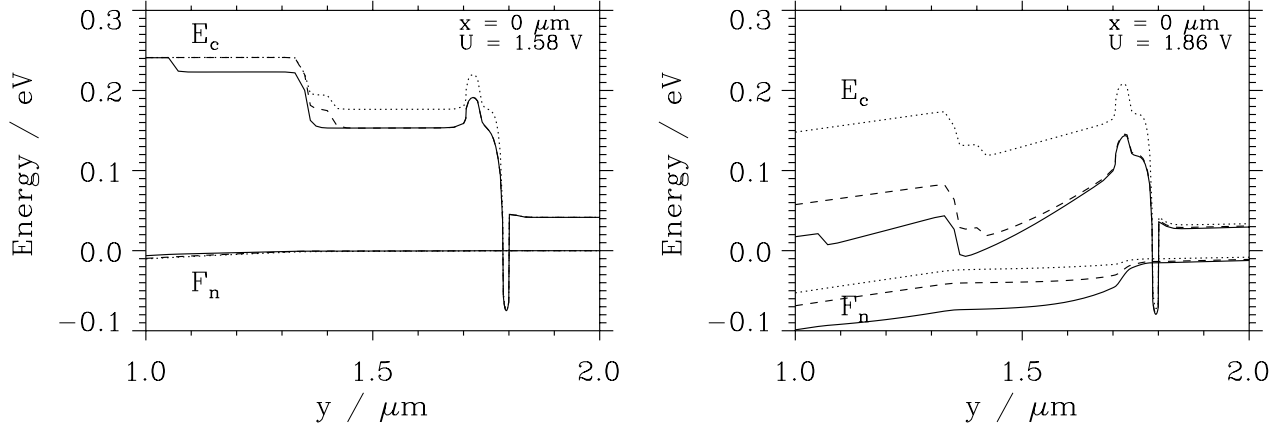


Figure 9: Conduction band edges and quasi-Fermi energies of the electrons perpendicular to the layers for the same p-doping profiles as in Fig. 8 near threshold ($U=1.58$ V, left) and at a power of 1 W in the laser cavity ($U = 1.86$ V, right). The active layer is at $y \approx 1.8 \mu\text{m}$, the p-doped waveguide layer at $1.7 \mu\text{m} > y > 1.4 \mu\text{m}$, and the p-doped cladding layer at $y < 1.4 \mu\text{m}$. Around $y = 1.75 \mu\text{m}$ there is a InGaP etch stop layer. Solid corresponds to moderate p-doping, dashed to a higher p-doping in the cladding layer only and dotted to higher p-doping in both cladding and waveguide layers.

In Fig. 10 we have summarized different possibilities to get more linear P-I characteristics. The first way is to try to keep the internal losses as small and the laser length as large as possible (dashed line). The second way is to enhance the acceptor density in the layers adjacent to the active layer (dotted line). Note, that in contrast to Fig. 8 where the losses were kept constant, α_0 has been increased in Fig. 10.

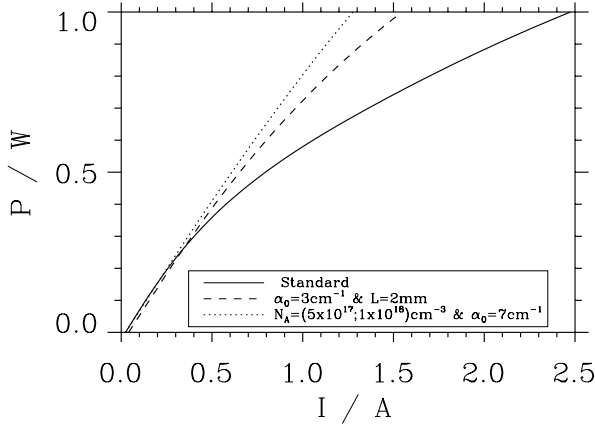


Figure 10: Output power of the RISAS laser versus current for different combinations of losses, laser length and p-doping profile. Solid: $\alpha_0 = 5 \text{ cm}^{-1}$ and $L = 1 \text{ mm}$, $N_A = 2 \cdot 10^{17} \text{ cm}^{-3}$ (waveguide), $N_A = 5 \cdot 10^{17} \text{ cm}^{-3}$ (cladding). Dashed: $\alpha_0 = 3 \text{ cm}^{-1}$ and $L = 2 \text{ mm}$, $N_A = 2 \cdot 10^{17} \text{ cm}^{-3}$ (waveguide), $N_A = 5 \cdot 10^{17} \text{ cm}^{-3}$ (cladding). Dotted: $\alpha_0 = 7 \text{ cm}^{-1}$ and $L = 1 \text{ mm}$, $N_A = 5 \cdot 10^{17} \text{ cm}^{-3}$ (waveguide), $N_A = 1 \cdot 10^{18} \text{ cm}^{-3}$ (cladding).

4.2. ARROW laser

The ARROW laser structure, depicted in Fig. 11, consists of a single compressively strained InGaAs QW (*cf.* Section 3.) sandwiched by GaAs spacer layers, InGaAsP waveguide and InGaP cladding layers. The aim of the lateral n-GaAs is again two-fold: Due to its *higher* refractive index than the surrounding material, it provides anti-index guiding in the lateral

direction, and due to the reverse biased pn-junction, partial current confinement is achieved. The current flow is further restricted by the He-implanted region shown hatched in the right figure. The influence of both the reverse biased pn-junction and the He-implanted region modeled by a factor 10^{-3} smaller mobilities is clearly seen in the contour plot of the hole quasi-Fermi energy (left part of Fig. 11). It is interesting to note, that obviously holes are laterally injected into the n-GaAs layer having a smaller band gap than the surrounding material.

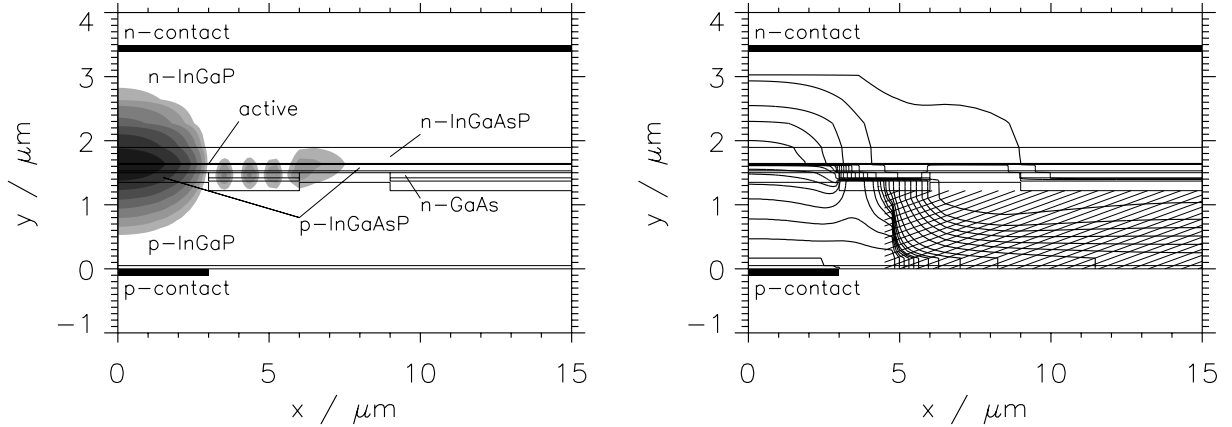


Figure 11: Cross-section of the optimized ARROW laser and distributions of the intensity of the fundamental lasing mode (left) and the hole quasi-Fermi energies (right) near threshold. The high index ARROW reflector is located between $x/\mu\text{m} = 3 \dots 6$ and the low index ARROW reflector between $x/\mu\text{m} = 6 \dots 9$. In the left gray-scale plot, the darkest region corresponds to the highest mode intensity which changes by a factor of 1/2 from contour line to contour line. In the right part, contour lines are drawn between -1.4 eV at the p-contact and -1.3 eV in non-equidistant steps. The He-implanted region is shown hatched.

Comparing Figs. 2 and 11, one can see that the lateral structure of the ARROW laser is much more complicated. Besides the central core (total width $W_1 = 6 \mu\text{m}$), there are two additional lateral reflectors, one having a higher effective index and the other one having a lower effective index. By proper choice of the widths W_2 and W_3 of these reflectors, the main maximum of a certain mode (which is not the fundamental mode of the associate waveguide) is located in the central core as shown in the right gray-scale plot of Fig. 11. Because this mode starts lasing first, we call it fundamental lasing mode. In general, $W_3 = W_1/2$ must hold,⁵ whereas the optimum values for W_2 depend on the effective index step chosen (in our case approximately $-5 \cdot 10^{-2}$). In our case, $W_2 = 3 \mu\text{m}$ is nearly an optimum. Another optima (with respect to threshold current and external efficiency) would be around $W_2 = 1.3 \mu\text{m}$ and $W_2 = 2.2 \mu\text{m}$, the latter however with a double-lobed farfield. Figs. 12 and 13 display the effects of a variation of W_2 .

In Fig. 12 calculated P-I characteristics for different values of the width W_2 of the high-index reflector are shown. We note, that in this figure the differential refractive index n_r' was set to zero. Due to the strong built-in index step of our example device, this has only minor influence on the P-I characteristic. As one can see from Fig. 12 the value of W_2 has to be carefully adjusted. The reason why the threshold current and the bending of the P-I characteristic is much larger for $W_2 = 3.4 \mu\text{m}$ can be seen by comparing the left part of Fig. 11 and Fig. 13: There is an additional side maximum in the high-index reflector and the intensity in the low-index reflector is much higher. Therefore, the overlap of the mode intensity with the excess carrier densities is weaker leading to a higher contact voltage needed to reach threshold. Note, that the appearance of an additional intensity maximum is connected with a change in the far field, in this case from a single-lobe far field to a double-lobe one.

In Fig. 14 the fundamental lasing mode power, where the modes displayed in Fig. 15 start to lase, is shown as a function of the internal losses. Note, that in contrast to the RISAS laser (*cf.* Fig. 6) the kink power increases with increasing loss. The reason is a defocusing of the non-lasing modes due to the carrier-induced index depression as already found using a simpler model based on the effective index method (EIM).¹⁹ The kink power calculated with our model is not as high as expected from calculations using the EIM. The reasons could be the following. First, we solve Eq. (4) subject to the condition of a vanishing electric field at the outer boundaries of the device. This forces the existence of proper modes. But in ARROW structures, if the imaginary part of the dielectric function ϵ is neglected, actually only leaky modes exist. The difference

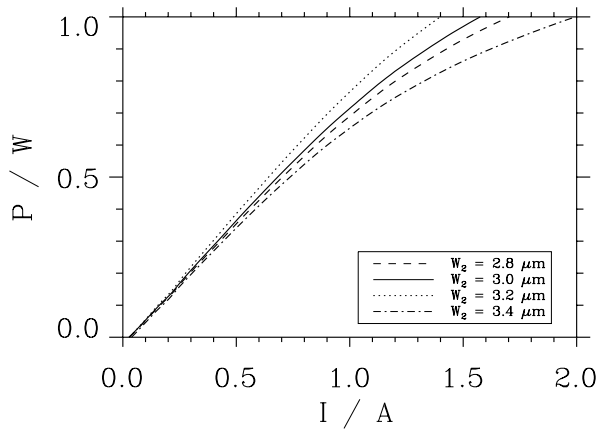


Figure 12: Output power of the ARROW laser versus current for different values of the width W_2 of the high index reflector.

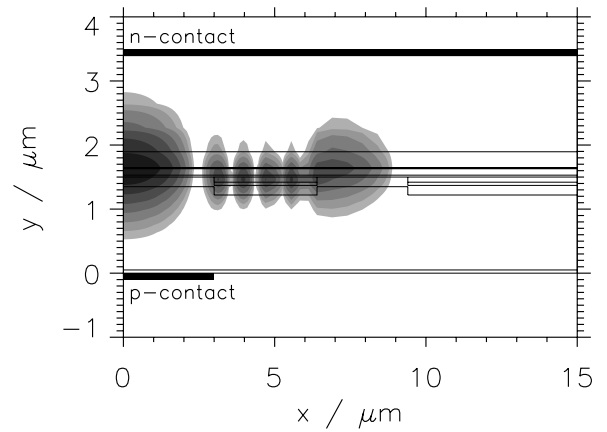


Figure 13: Gray-scale plot of the intensity distribution of the fundamental lasing mode for $W_2 = 3.4 \mu\text{m}$.

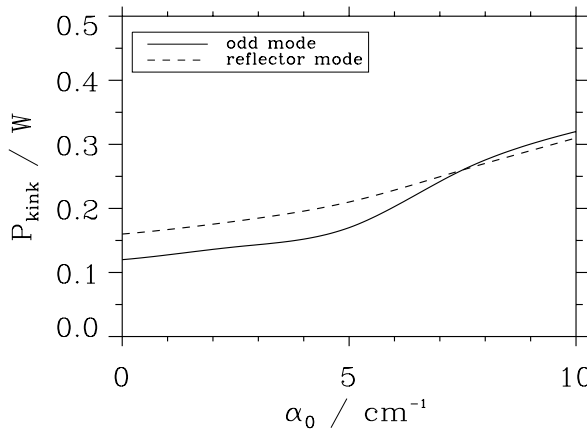


Figure 14: Fundamental lasing mode power where the modes displayed in Fig. 15 start to lase versus internal losses common for all modes. Solid: Odd mode corresponding to the left plot of Fig. 15. Dashed: Reflector mode corresponding to the right plot of Fig. 15.

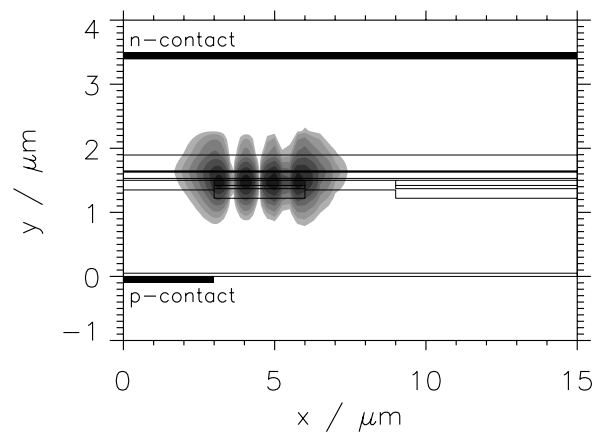
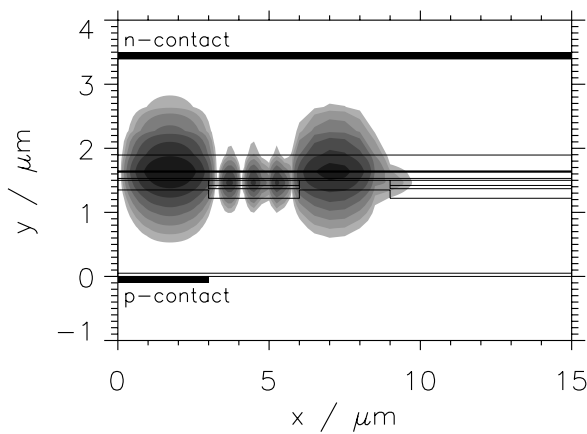


Figure 15: Gray-scale plots of the intensity distributions of ARROW modes possibly competing with the lasing mode at higher output power. Left: Odd mode. Right: Reflector mode.

between a proper and a leaky mode is, that the propagation constant of the latter takes a complex value the imaginary part of which is proportional to the radiation loss. In contrast to the FEM, with the EIM this can be easily accounted for. Therefore, the smaller kink power obtained with our FEM model could be explained by the neglect of the radiation loss which is much larger for the higher order modes than for the fundamental lasing mode. On the other hand, because the EIM is only an approximate method, it is questionable whether it is applicable to higher order ARROW modes or not. Therefore, it could be that the kink power obtained with the EIM is not reliable. Using a sophisticated three dimensional finite integration beam propagation model²⁰ we plan to investigate this discrepancy in more detail. Note that by introducing higher losses for the non-lasing modes as done in Fig. 6 the kink power can be easily shifted to larger values.

5. SUMMARY

We have introduced a new scheme for simulating the light-current characteristics of single-mode high-power lasers. It allows us to treat transverse and longitudinal spatial holeburning on equal footing and to model current flow and waveguiding high above threshold. We found that using the InGaAsP/GaAs material system for lasers emitting around 800 nm necessitates a careful optimization. Both RISAS and ARROW lasers have the capability to yield single-mode output powers of more than 500 mW if the higher order modes experience somewhat higher losses than the fundamental lasing mode.

6. ACKNOWLEDGMENT

The authors wish to thank H. Gajewski (WIAS Berlin) for providing the simulator ToSCA, R. Nürnberg (WIAS Berlin) for technical support, H.-J. Wünsche (HUB) for many collaborations involving this subject, and M. Weyers (FBH) for a critical reading of the manuscript. This work was supported by the Bundesministerium für Bildung und Forschung under contract 13 N 6375.

7. REFERENCES

- [1] H. Asonen, A. Ovtchinnikov, G. Zhang, J. N. Näppi, P. Savolainen, and M. Pessa, "Aluminum-free 980-nm GaInAs/GaInAsP/GaInP pump lasers", *IEEE J. Quantum Electron.*, vol. 30, pp. 415-423, 1994.
- [2] M. Ohkubo, T. Ijicho, A. Iketani, and T. Kiluta, "980-nm aluminum-free InGaAs/InGaAsP/InGaP GRIN-SCH SL-QW lasers", *IEEE J. Quantum Electron.*, vol. 30, pp. 408-414, 1994.
- [3] E.C. Vail, R. F. Nabiev, and C. J. Chang-Hasnain, "Temperature dependence of light-current characteristics of 0.98- μ Al-free strained-quantum-well lasers", *IEEE Photon. Technol. Lett.*, vol. 6, pp. 1303-1305, 1994.
- [4] O. Imafuji, T. Takayama, H. Sugiura, M. Yuri, H. Naito, M. Kume, and K. Itoh, "600 mW CW Single-mode GaAlAs triple-quantum-well laser with a new a new index guided structure", *IEEE J. Quantum Electron.*, vol. 29, pp. 1889-1894, 1993.
- [5] L.J. Mawst, D. Botez, C. Zmudzinski, and C. Tu, "Design optimization of ARROW-type diode lasers", *IEEE Photon. Technol. Lett.*, vol. 4, pp. 1204-1206, 1992.
- [6] H.J. Wünsche, U. Bandelow, and H. Wenzel, "Calculation of combined lateral and longitudinal spatial hole burning in $\lambda/4$ shifted DFB lasers", *IEEE J. Quantum Electron.*, vol. 29, pp. 1751-1760, 1993.
- [7] G. H. Song, *Two-dimensional simulation of quantum-well lasers including energy transport*, Ph.D. dissertation, University of Illinois, Urbana-Champaign, 1990.

- [8] Z.-M. Li, K. M. Duzurko, A. Delage, and S.P. McAlister, "A self-consistent two-dimensional model of quantum-well semiconductor lasers: Optimization of a GRIN-SCH SQW laser structure", *IEEE J. Quantum Electron.*, vol. 28, pp. 792-803, 1992.
- [9] G.-L. Tan, N. Bewtra, K. Lee, and J. M. Xu, "A two-dimensional nonisothermal finite element simulation of laser diodes", *IEEE J. Quantum Electron.*, vol. 29, pp. 822-835, 1993.
- [10] M. Gault, P. Mawby, A. R. Adams, and R. Towers, "Two-dimensional simulation of constricted-mesa InGaAsP/InP burier-heterostructure lasers", *IEEE J. Quantum Electron.*, vol. 30, pp. 1691-1700, 1994.
- [11] H. Gajewski, B. Heinemann, H. Langmach, G. Telschow, and K. Zacharias, *ToSCA Handbuch*, Berlin: Weierstraß-Institut für Angewandte Analysis und Stochastik, 1991.
- [12] H.J. Wünsche, H. Wenzel, U. Bandelow, J. Piprek, H. Gajewski, and J. Rehberg, "2D Modeling of distributed feedback semiconductor lasers", in *Proc. 4th Int. Conf. on Simulation of Semicond. Dev. Processes*, W. Fichtner and D. Ammer, Eds. Konstanz: Hartung-Gorre, 1991, pp. 65-70.
- [13] H. Wenzel and H.-J. Wünsche, "A model for the calculation of the threshold current of SCH-MQW-SAS lasers", *phys. stat. sol. (a)*, vol. 120, pp. 661-673, 1990.
- [14] J. Piprek, H. Wenzel, *et al.*, "Modeling light vs. current characteristics of long-wavelength VCSELs with various DBR materials", *SPIE Phys. Simul. Optoelectr. Dev. III*, vol. 2399, pp. 605-616, 1995.
- [15] C.G. Van de Walle, "Band lineups and deformation potentials in the model-solid theory", *Phys. Rev. B*, vol. 39, pp. 1871-1883, 1989.
- [16] J. Diaz, I. Eliashevich, *et al.*, "Theoretical investigation of minority carrier leakages of high-power 0.8 μm InGaAsP/InGaP/GaAs laser diodes", *Appl. Phys. Lett.*, vol. 65, pp. 2260-2262, 1994.
- [17] H. Wenzel, Unpublished.
- [18] F. Bugge, G. Beister, G. Erbert, S. Gramlich, I. Rechenberg, H. Treptow, and M. Weyers, "Effect of growth interruption on performance of AlGaAs/InGaAs/GaAs quantum well lasers", *J. Crystal Growth*, vol. 145, pp. 907-910, 1994.
- [19] L.J. Mawst, D. Botez, R.F. Nabiev, and C. Zmudzinski, "Above-threshold behavior of high-power single-mode antiresonant reflecting optical waveguide diode lasers", *Appl. Phys. Lett.*, vol. 66, pp. 7-9, 1995.
- [20] M. Niederhoff, H. Wenzel, W. Heinrich, and P. Russer, "Assessment of numerical methods for calculating the optical field distributions in ARROW structures", *Microwave and Optronics Conference*, Sindelfingen 1995.